

## ARTICLE OPEN



# Atmospheric rivers impacting western North America in a world with climate intervention

Christine A. Shields<sup>1</sup>✉, Jadwiga H. Richter<sup>1</sup>, Angeline Pendergrass<sup>1,2</sup> and Simone Tilmes<sup>1</sup>

Atmospheric rivers (ARs) impacting western North America are analyzed under climate intervention applying stratospheric aerosol injections (SAI) using simulations produced by the Whole Atmosphere Community Climate Model. Sulfur dioxide injections are strategically placed to maintain present-day global, interhemispheric, and equator-to-pole surface temperatures between 2020 and 2100 using a high forcing climate scenario. Three science questions are addressed: (1) How will western North American ARs change by the end of the century with SAI applied, (2) How is this different from 2020 conditions, and (3) How will the results differ with no future climate intervention. Under SAI, ARs are projected to increase by the end of the 21st century for southern California and decrease in the Pacific Northwest and coastal British Columbia, following changes to the low-level wind. Compared to 2020 conditions, the increase in ARs is not significant. The character of AR precipitation changes under geoengineering results in fewer extreme rainfall events and more moderate ones.

*npj Climate and Atmospheric Science* (2022)5:41 | <https://doi.org/10.1038/s41612-022-00260-8>

## INTRODUCTION

Atmospheric rivers (ARs) play a crucial role in Earth's hydrological cycle by transporting moisture via long, narrow, synoptic-scale weather features often associated with extratropical cyclones<sup>1</sup>. Coastlines along the westernmost portions of continents, and in particular, western North America, are disproportionately impacted by ARs compared to interior continental areas because much of the moisture, either remotely or locally sourced, begins to dry as the storm system moves inland<sup>2–4</sup>. For western North America, AR moisture is primarily forced upward through orographic lift as the AR collides with the mountain ranges, such as Sierra Nevada and Cascades, thus providing the physical mechanism to produce significant precipitation<sup>5–7</sup>. Regions such as California receive over half of their annual precipitation through ARs<sup>8,9</sup>, with precipitation ranging from beneficial, drought-relieving rain to destructive events that initiate extreme flooding<sup>10–13</sup>. As the climate continues to warm, ARs are expected to grow in size and contain a higher moisture content, potentially worsening floods and increasing extreme events<sup>2,14–17</sup>. Understanding how ARs change in the future is critical for managing water resources in local communities.

Solar geoengineering, in particular stratospheric aerosol injection (SAI), has been debated as a possible intervention method to reduce some of the worst effects of global warming. In recent years, it has become clear that reaching important climate targets will be increasingly difficult due to the continued use of fossil fuels and subsequent increase in greenhouse gas emissions. Scientific debate on the wisdom of climate intervention strategies has populated the scientific literature for over a decade<sup>18–21</sup>. SAI has been proposed to have the potential to mitigate the effects of climate change until greenhouse gas concentrations can be sufficiently reduced. However, large uncertainties still exist in our understanding of the impacts of these methods. Do the risks and dangers of engineering a solution to combat serious climate change impacts outweigh the benefits of such an exercise? To answer this question, first, we must fully understand the consequences of different climate intervention strategies. The recent National Academies of Sciences, Engineering

and Medicine (NASEM) report on solar geoengineering research and governance<sup>22</sup> concluded that studies done to date do not provide a sufficient basis for supporting informed decisions and recommends research to better characterize and reduce uncertainties concerning benefits and risk of solar geoengineering deployment. One set of tools at our disposal are Earth System Models (ESMs) as evidenced by the GeoMIP (Geoengineering Model Intercomparison Project) effort, where different modeling centers around the world applied the same climate engineering scenarios to their ESMs in order to assess climate projections<sup>23</sup>. Due to the participation of varying ESM-complexity, some GeoMIP experiments have been simplified and utilized solar constant reduction or a prescribed aerosol distribution<sup>24,25</sup>. In addition, even the more complex experiments performed stratospheric injections at the equator which have led to overcooling of the tropics and undercooling of the poles<sup>26</sup>. Kravitz et al.<sup>27</sup> presented the first simulation of solar geoengineering using multiple locations of sulfur dioxide (SO<sub>2</sub>) injections (15°S, 15°N, 30°S, 30°N), with the amount of SO<sub>2</sub> varying from year to year to meet three simultaneous temperature objectives. This approach significantly reduced the overcooling/undercooling patterns noted in previous studies as global mean temperature, the pole-to-pole temperature gradient, and the interhemispheric temperature gradients were kept near 2020 levels. Here we utilize simulations from the Geoengineering Large Ensemble (GLENS)<sup>28</sup>, which used the approach by Kravitz et al.<sup>27</sup> of time-varying SO<sub>2</sub> point injections at the four different latitudes, 5 km above the tropopause in the stratosphere in a 20-member ensemble of century long simulations. By utilizing large ensembles, we can robustly simulate the climate and better represent internal variability<sup>29,30</sup> (Deser et al., 2014, Kay et al., 2105). The global mean temperature, inter-hemispheric temperature gradient, and the equator-to-pole temperature gradient in GLENS simulations with SO<sub>2</sub> injections remain very close to 2020 levels (Supplementary Fig. S1).

The GLENS project<sup>28</sup> has produced many studies highlighting both the benefits and unintended consequences of injecting sulfate aerosol as a means to mitigate climate change<sup>28,31–38</sup>.

<sup>1</sup>National Center for Atmospheric Research, Boulder, CO 80302, USA. <sup>2</sup>Cornell University, Earth and Atmospheric Science, Ithaca, NY 14850, USA. ✉email: shields@ucar.edu

Jiang et al.<sup>34</sup> explained how SAI could potentially impact the high latitude seasonal cycle, and Fasullo et al.<sup>33</sup> warned of a warmer polar ocean forced by an accelerated Atlantic Meridional Overturning Circulation (AMOC). Here, we apply GLENS to investigate SAI impacts on the Pineapple Express variety of ARs important for western North American hydroclimate. Simpson et al.<sup>36</sup> discussed the hydroclimate response to geoengineering in GLENS for specific regions worldwide and showed that wintertime westerlies in the Pacific shift equatorward with wetting in the southwest U.S. Although some of these broad aspects of the hydrological cycle have been studied under geoengineered conditions with both GeoMIP and GLENS efforts, to our knowledge, very little has been focused on western North America and atmospheric rivers, which could potentially explain the hydroclimate response in Simpson et al.<sup>36</sup>. For western North America, ARs often combine extratropical cyclone dynamics with long and narrow plumes of moisture transported along the cold frontal boundary to produce precipitation primarily during the cool and wet season along the coast<sup>5–7,39</sup>. Given that U.S. West Coast communities, such as California, depend on the water resources delivered by ARs, examining how geoengineering could impact these water resources is critical for planning and future adaptation<sup>18</sup>.

Here, we diagnose how stratospheric sulfate injection impacts the dynamics forcing atmospheric rivers and their associated precipitation, specifically for western North America. We present analysis of simulations with and without SAI analysis averaged over a 20-year period at the end of the century, after steadily increasing SO<sub>2</sub> injections from 2020 through 2100, and compare to the RCP8.5 scenario, both at the end of the century, to highlight the impact of SAI, and near-term, to highlight how different the climate will be compared to today. Comparing both of these perspectives to the RCP8.5 scenario will also illustrate how geoengineering utilizing SO<sub>2</sub> injection compares to no climate mitigation whatsoever. Table 1 names each analysis period and provides the reference dates, i.e., geoengineering versus RCP8.5 at the end of the century GLENS (EC) vs RCP85 (EC), geoengineering versus RCP8.5 in the near term, i.e., the “control”, GLENS (EC) vs BASE, and RCP8.5 scenario versus the near-term control, RCP8.5 (EC) vs BASE.

## RESULTS AND DISCUSSION

### Background climate

Surface annual temperature and precipitation are shown in Fig. 1 to illustrate the background climate state differences between each analysis period. Simulations with SAI successfully reduce the global annual surface temperature compared to RCP8.5 (Fig. 1a, c), with little difference compared to the near term (Fig. 1c), in particular, over continental locations. Precipitation is more complicated. In general, annually averaged values tend to be wetter in RCP8.5 world compared to a geoengineered world (Fig. 1d–f) which is consistent with the basic constant RH warming response, in which moisture availability in the atmosphere increases by about 6–7% per degree of warming. By combining atmospheric moisture with wind patterns, we also show integrated water vapor (IVT) pathways typical for atmospheric rivers (Fig. 1g–i). IVT is calculated by vertically

integrating specific humidity and zonal and meridional winds throughout the atmosphere<sup>40</sup>. These annual mean IVT pathways are quite different across the analysis scenarios and provide context for a more detailed AR analysis that follows. In the next sections, we will show the complex nature of the precipitation response (and change for ARs) and the importance of considering season, location, and the underlying mechanism delivering that precipitation.

**Dynamical forcing.** Atmospheric rivers are often considered a subset of the extratropical cyclone whose motions are determined by the steering flow and subsequent jetstreams, both eddy-driven and subtropical. Consistent across generations of climate models, it is well understood that the storm track is generally projected to move poleward as the climate warms<sup>41–43</sup>, although regional variability exists<sup>44,45</sup>. Changes in atmospheric river tracks, and therefore the location of landfall, will follow suit, and simply follow the dynamical forcing which has been shown for both future and paleoclimates<sup>46–48</sup>. For a geoengineered world, where SAI lowers the surface temperatures, the expectation would be that AR landfalls, and therefore modifications to winter precipitation patterns, will again respond to the dynamics, which it does. The jetstream is a vector quantity, with both meridional and zonal components. In the mid-latitudes, the main location for AR activity<sup>40</sup>, the zonal wind component is dominant and can be used as a proxy for the steering flow. Comparing the end of the century SAI response to the RCP8.5 scenario (Fig. 2a, b) the cool-season zonal wind (U) decreases in strength for most of the troposphere in the 40°–60°N and increases in strength for latitudes < ~40°N, with statistical significance computed at the 95th percentile. This is consistent with Simpson et al.<sup>36</sup> (Fig. 5b) that showed an equatorward shift in the 850 hPa zonal winds when geoengineering was applied. Focusing on the lower atmospheric levels, where the vast majority of the moisture is transported, and decomposing changes in strength by month (Fig. 3d, e), a more nuanced pattern emerges by season, typical of the seasonality of winds driven by the solar heating and thermal wind<sup>49</sup>. Taking the same diagnostic approach to illustrate AR frequency changes by season and latitude (Fig. 3a, b), the rate of AR change patterns (scaled to percent change relative to the reference period) reflect the 700 hPa level zonal wind changes for the respective analysis periods. Significance in AR frequency, denoted by black stars, is defined as no overlap between ensemble members between the comparison periods, i.e., for Fig. 3a, where all SAI, GLENS ensembles at the end of the century are either greater (or fewer) than all RCP8.5 ensembles members at the end of the century. For reference to a world with no geoengineering and RCP8.5 emissions, (Figs. 2c and 3c, f), the relationship between zonal wind and AR frequency is the same, however the signal itself is generally opposite of the SAI simulations. For these GLENS simulations, the AR changes are only significant for the end of century comparisons (Fig. 3a, c) for the shoulder and summer seasons with little significance for the SAI compared to near-term (Fig. 3b). It should also be noted that the high relative change in the summer months does not equate to a high absolute change in frequency (Supplementary Table S2), but a change from little or no instances to several more events. In general, for lower mid-latitudes, geoengineering simulations tend

**Table 1.** Simulation analysis periods for Geoengineering (GLENS) and RCP8.5 scenarios.

Analysis scenario	GLENS analysis period	RCP8.5 analysis period(s)
GLENS vs RCP8.5	EC (2080–2097)	EC (2080–2097)
GLENS vs BASE	EC (2080–2097)	BASE (2010–2030)
RCP8.5 vs BASE	N/A	EC (2080–2097) vs BASE (2010–2030)

BASE is considered the control in the near-term and EC refers to the end of the century.

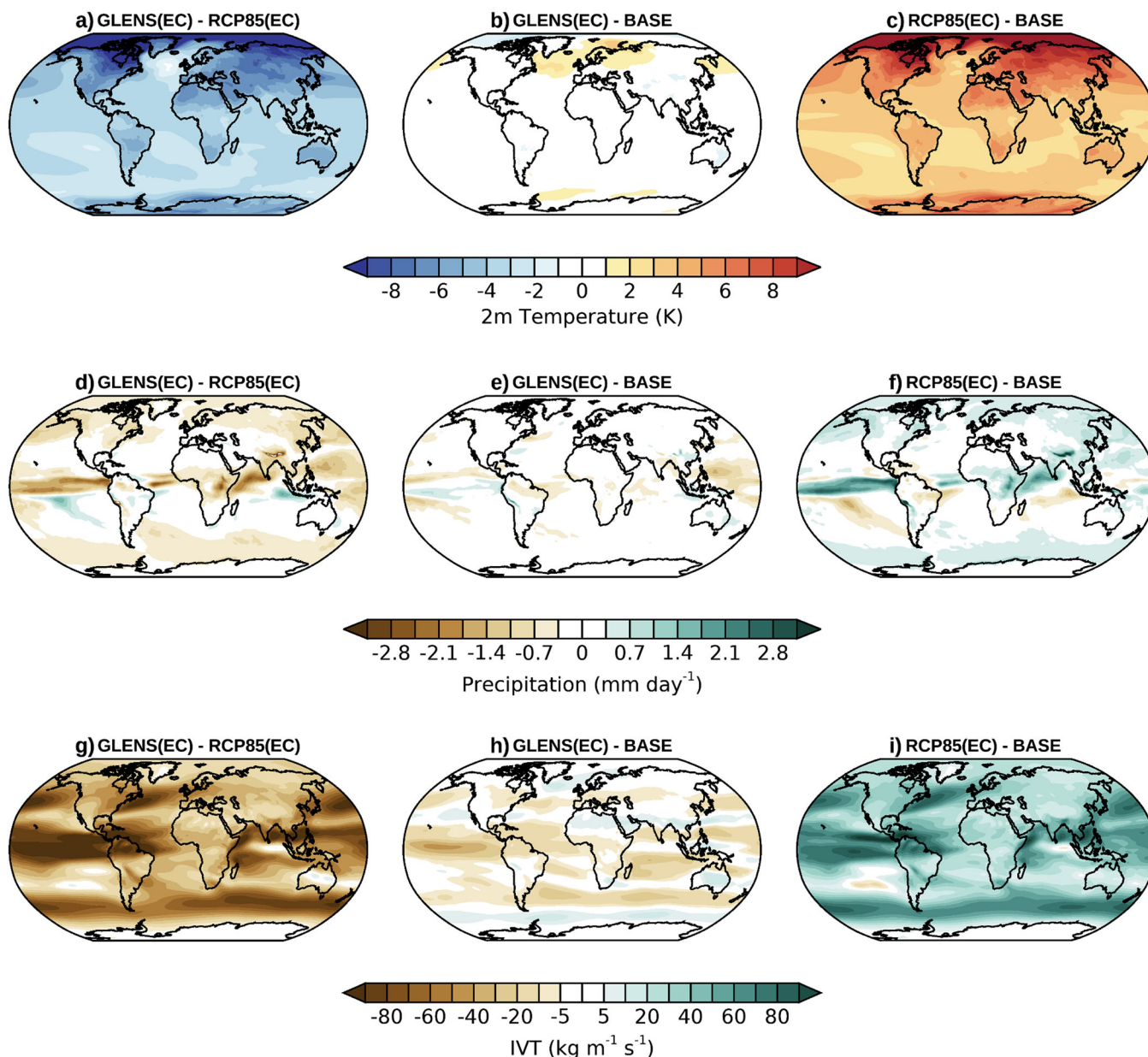


**Fig. 1 Background climate for analysis scenarios.** Annually averaged surface air temperature (a–c), total precipitation (d–f), and integrated vapor transport (g–i) differences for the three analysis periods (GLENS - RCP8.5, end of century (EC) a, d, g; GLENS - RCP8.5, EC and BASE (b, e, h), respectively; RCP8.5, EC - BASE, c, f, i). Surface temperature is in °C, precipitation is in  $\text{mm day}^{-1}$ , and integrated vapor transport is in  $\text{kg m}^{-1} \text{s}^{-1}$ .

towards an increase in ARs with the opposite under RCP8.5, as supported by the low-level winds in Figs. 2 and 3.

**Precipitation.** Precipitation attributable to ARs is an important metric to consider when assessing climate change impacts. If ARs shift, so will the precipitation and thereby an important water source for many communities. Before understanding changes in precipitation due to ARs, first, a look at total precipitation is needed. Figure 4 demonstrates changes to precipitation for the three analysis scenarios we have evaluated thus far. From the geoengineered climate perspective, total cool season precipitation north of  $35\text{--}40^\circ\text{N}$  is dramatically drier in an ensemble mean (Fig. 4a) compared to an RCP8.5 (Fig. 4c) world. To see the impact of a geoengineered world compared to our present-day climate (i.e., BASE), Fig. 4b hints that precipitation in the southern California region would be increased under SAI conditions, and the Pacific Northwest would be drier.

Given that the dominant precipitation over California in the cool season is due to ARs, this prompts the question as to whether or not ARs can explain this signal. The ratio of AR precipitation to total precipitation remains relatively consistent across different climate regimes and latitude bands over western North American, where southern California has the highest contributions from ARs (up to 42%) and the Pacific Northwest has the lowest contributions (under 10%) across all ensemble members (Supplementary Fig. S2). For reference, additional similarly styled cool season precipitation can be found in the supplemental for (1) the GLENS historical simulations (Supplementary Fig. S3), (2) moisture and wind variables key to AR formation, i.e., IVT, IWV, and low-level winds (Supplementary Fig. S4), and (3) median, maximum, and minimum precipitation years (Supplementary Fig. S5).

By evaluating precipitation distributions across all three of our analysis scenarios, we gain insight into the character of precipitation

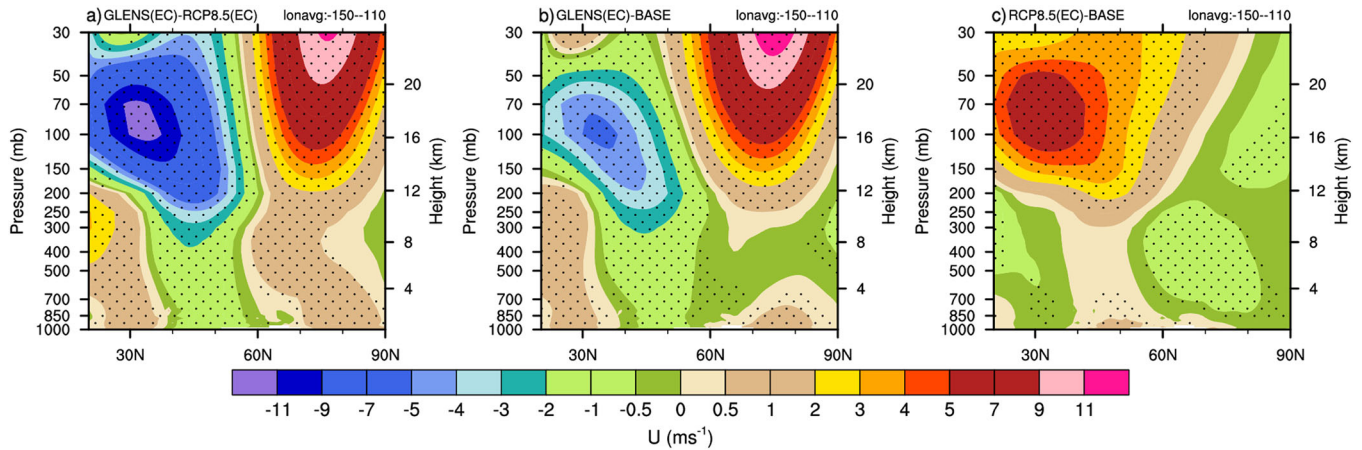


**Fig. 2 Cool season zonal wind for analysis scenarios.** Cool season (October–March) mean zonal wind ( $U$ ) changes for three analysis periods averaged over 110–150°W. GLENS (EC) - RCP8.5 (EC) (a), GLENS (EC) - BASE (b), RCP8.5 (EC) - BASE (c). Stippling is computed at 95% significance with a Student's  $T$  test.

as illustrated in Fig. 5. We give each analysis scenario a different color-theme to highlight the differences in the respective, relative responses. Under geoengineering (GLENS), the distribution of precipitation shifts from high into more moderate rainfall rates (Fig. 5a–d, blue curves) compared to the RCP8.5 end of century climate (black/gray) curves for all latitude bands, although the largest shifts and increases are in the lower latitudes. Significance (star markers plotted over the respective rain rate bins) is defined as no overlap between the ensemble spread (shaded) between different climate scenarios. The character of the precipitation changes by region is illustrated by breaking down the precipitation distributions into latitude bands. There are a number of significant changes in the end of the century GLENS as well as the RCP8.5 world (Fig. 5i–l). Under the RCP8.5 climate by the end of the century (red in Fig. 5i–l and black/gray in Fig. 5a–d), more extreme precipitation rates exist, compared to the geoengineered world (blue in Fig. 5a–d and brown/tan in Fig. 5e–h). There is however a lack of significance for the geoengineered world (GLENS) compared to our near-term climate (BASE). Although the geoengineered world hints at an increase in precipitation consistent with total precipitation (Fig. 4b), the lack of significance and small differences in distribution suggest that at least AR precipitation intensity in a geoengineered world could be similar to today.

Finally, to characterize the seasonal phasing of AR precipitation, we calculate the climatological mean water year for each ensemble spread and compare across our analysis scenarios (Fig. 6). Accumulated precipitation is plotted for the ensemble spread (shading) for each month of the year. Across all scenarios and ensemble members, the GLENS simulations accumulate the majority of the yearly precipitation falling between October and March, consistent with timing of most AR landfall events. For GLENS (EC) compared to RCP8.5 (EC), (Fig. 6a–d), the range of water year accumulations by ARs has clearly narrowed for lower latitudes, closest to subtropical jet and strongest low-level flow, and where highest precipitation rates occur. For GLENS (EC) scenario compared to the near-term climate (BASE), most latitudes exhibit a similar distribution and little change with the exception for the lowest latitudes (Fig. 6e–h). The increase in total accumulated precipitation suggests that even though precipitation rate differences between these scenarios (Fig. 5e) are effectively the same, AR-precipitation throughout the year does increase for Southern California latitude bands.

AR precipitation is projected to shift from higher to more moderate intensity bands in geoengineering simulations with SAI that were carried out as part of GLENS. The impact is highest for the southern half of California, but much smaller than without

intervention. In particular, where (1) ARs dominate as a precipitation source and (2) precipitation is projected to become more intense with much higher rainfall rates in a future warmer world compared to the near-term climate. The benefit of SAI is most keenly felt by the end of the century when the increase in surface temperature is greatest, measured globally, across the hemispheres, and from equator to pole. When comparing SAI at the end of the century to a climate similar to today, the change in the character of the AR precipitation is not significantly different from our current world. In other words, geoengineering also appears to accomplish keeping the majority of AR precipitation intensity at moderate levels for much of the U.S. West Coast. However, it is equally important to understand that although the AR precipitation may not suffer under the application of geoengineering, this does not account for all precipitation. Total cool season precipitation (Fig. 4) suggests that even compared to the near-term, the spatial pattern of precipitation changes overall such that the Pacific Northwest and coast of British Columbia could potentially be negatively impacted with less precipitation under SAI, unrelated to ARs. One explanation is that extratropical cyclones change, shift, and/or produce less precipitation compared to the near-term climate. As ARs are a subset of extratropical cyclones, (abbreviated to ETCs), not all ETCs are ARs. A healthy debate on the definition of the ARs still persists in the AR research community<sup>1,39,50,51</sup> as evidenced by the many ARDTs that exist. ETCs generate precipitation through lift via the warm conveyor belt that brings warm, moist air up and over the warm frontal component<sup>52</sup>. This locally sourced precipitation is not considered in this study given the ARDT applied here (see Methods section below) specifically focuses on ARs with subtropical moisture sources, i.e., “Pineapple Express” flavor of ARs. Delving into the mechanisms behind a change in ETC to the upper mid-latitudes of western North America is an important topic for future research.

Another important conclusion from this study is that, under geoengineering using SAI, changes in AR frequency vary seasonally and regionally and are forced by the low-level wind, consistent with previous studies under different future and paleoclimate scenarios<sup>46,47</sup>. Where the jet location goes, the ARs will follow. The dynamics are consistent with AR precipitation where the most significant AR frequency responses occur under SAI and RCP8.5 forcing at the end of the century. In these simulations, there are more ARs in the lower middle latitudes in the geoengineered world with the reverse true for the RCP8.5. Winter upper mid-latitudes have the opposite signal but little significance. For geoengineering compared to the near-term (BASE), AR frequency changes are generally more muted,

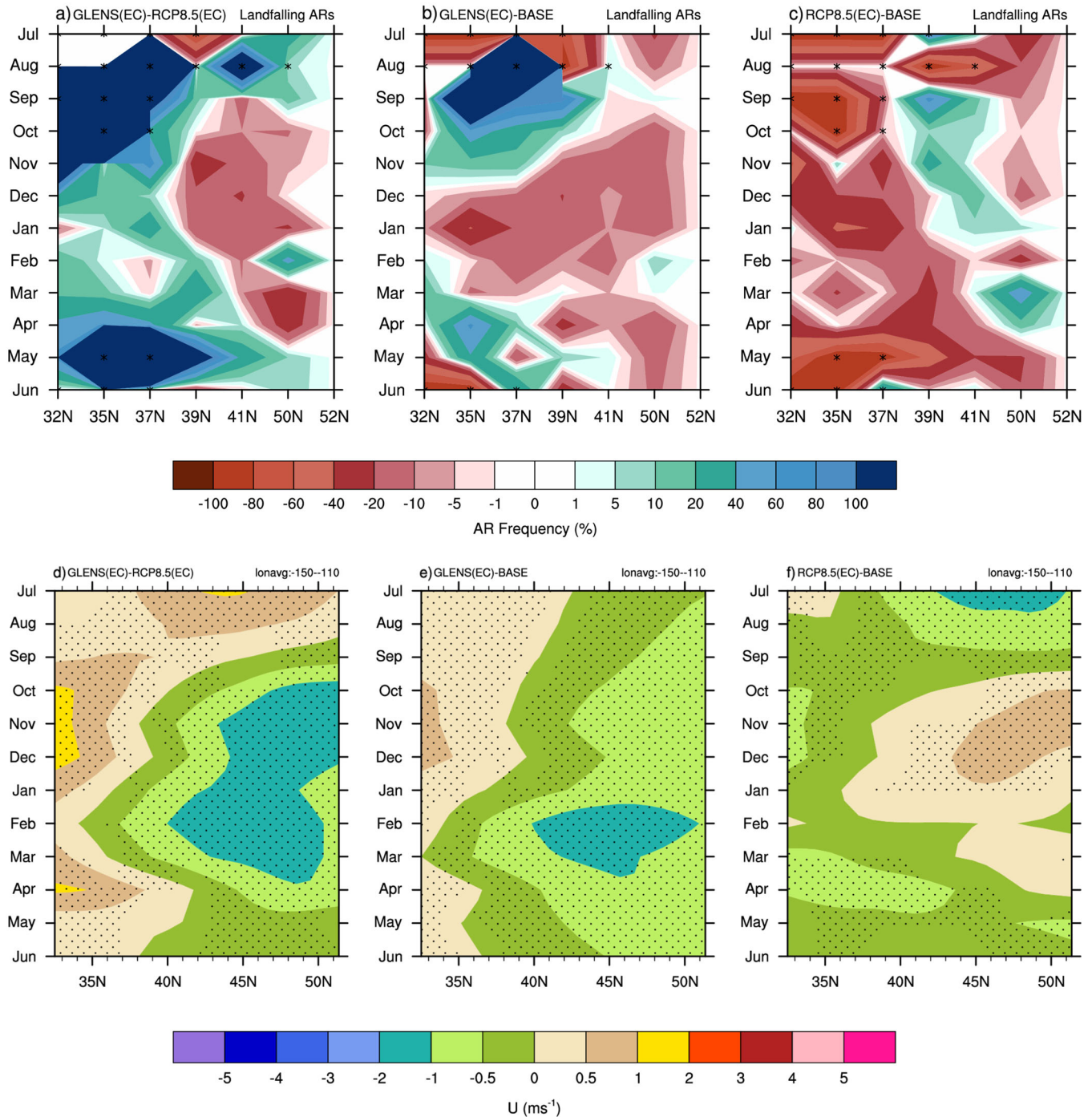


**Fig. 3 Low level jet changes drive AR frequency changes.** Climatological changes by latitude for ensemble mean AR frequency (a–c) and 700 hPa zonal wind (d–f) averaged over 110–150°W. GLENS (EC) - RCP8.5 (EC), (a, d); GLENS (EC) - BASE (b, e); RCP8.5 (EC) - BASE (c, f). Black lines for AR frequency plots indicate significance where there is no overlap between frequency values of different analysis periods, i.e., the spread of individual ensemble members is distinctly different for the analysis periods being compared. Frequency units are given as % of change relative to reference periods RCP8.5 (EC) (a), BASE (b, c). Stippling for 700 hPa zonal wind is computed at 95% significance with a Student's *T* test.

consistent with AR precipitation intensity. Southern California is the exception where water year diagnostics suggest that this region may experience more overall AR-precipitation compared to today. The spotty significance for AR frequency is in part, due to the number of years sampled (20 years at the end and beginning of the centuries) and the limited ensemble size of the end of century RCP8.5 simulations (3 ensemble members). However, given that (1) the low-level winds are the primary

mechanism delivering ARs to coastal regions of western North America, (Fig. 3d–f), and (2) this robust relationship agrees with previous studies focused on different climate regimes, our confidence is high that the changes to the 700 hPa winds reflect the mean AR climatology frequency changes as presented here.

In summary, geengineering utilizing SO<sub>2</sub> injections in the GLENS simulations carried out with CESM1(WACCM) shifts the low-level flow such that AR frequencies increase for southern California

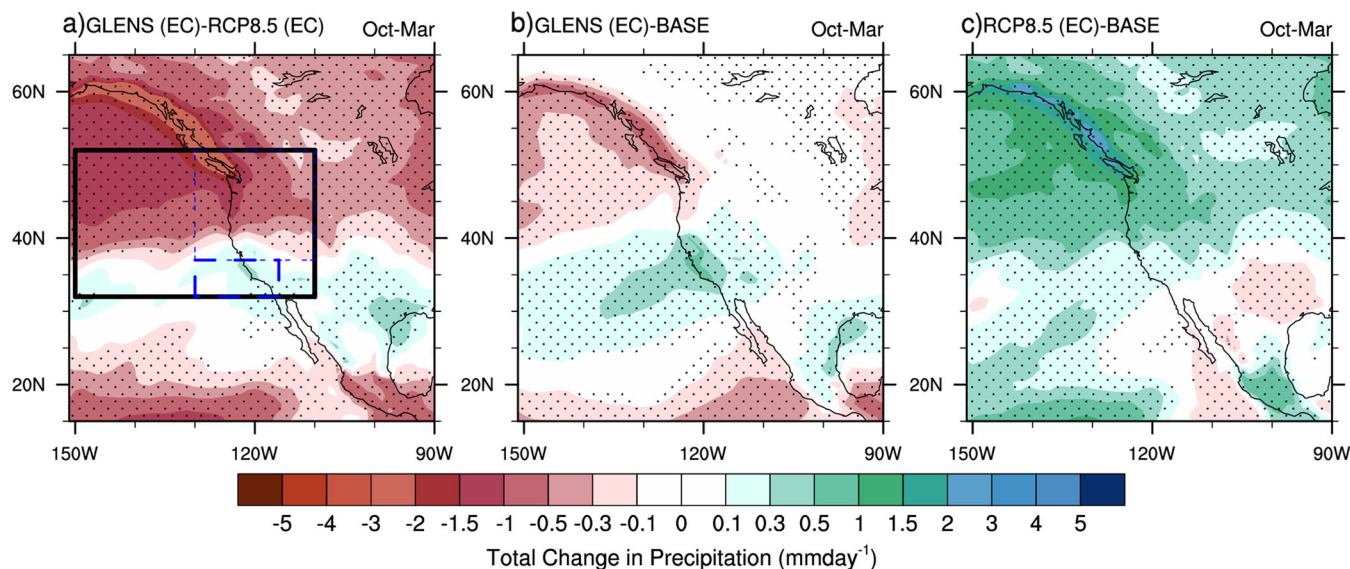


**Fig. 4 Cool season total precipitation for analysis scenarios.** Total precipitation change for cool season means (Oct–Mar). GLENS (EC) - RCP8.5 (EC) (a), GLENS (EC) - BASE (b), RCP8.5 (EC) - BASE (c). Precipitation units are  $\text{mm day}^{-1}$ . Stippling is computed at 95% significance with a Student's *T* test. The black box in a signifies the AR-dynamics analysis region (Figs. 2 and 3) with the blue boxes signifying AR-precipitation impacts regions (Figs. 5 and 6).

latitudes over most months of the year and decrease for the Pacific Northwest primarily for winter months. Precipitation attributable to ARs becomes less intense, with fewer extreme and more moderate precipitation rates. The most notable intensity differences occur when assessing geoengineering simulations at the end of the century compared to that of a RCP8.5 world. Compared to near-term climate, SAI does not appear to strongly change AR frequency, nor precipitation attributable to ARs for most latitudes, as these signals are more muted. Although ARs potentially explain, in part, the cool season precipitation signal for Southern California, it cannot explain this signal for elsewhere, and in particular, the upper mid latitudes including the Pacific Northwest and coastal British Columbia. Further research to address the limitations of this study (Methods section) and expand beyond “Pineapple Express” ARs is necessary to capture the full understanding and implications of SAI to atmospheric rivers.

## METHODS

### GLENS model and simulations

GLENS simulations were carried out with the Community Earth System Model, version 1 with the Whole Atmosphere Community Climate Model as its atmospheric component (CESM1(WACCM)). CESM1(WACCM) is a sophisticated, fully coupled (atmosphere, ocean, land, sea-ice) high top Earth System Model described fully in Mills et al.<sup>53</sup>. The atmosphere component of CESM1(WACCM) utilizes a horizontal grid  $0.9^\circ(\text{latitude}) \times 1.25^\circ(\text{longitude})$  and 70 vertical layers extending to 140 km ( $\sim 10\text{--}6$  hPa) in height. Tropospheric physics in CESM1(WACCM) are based on the Community Atmosphere Model, version 5 (CAM5<sup>54</sup>) with improvements to the representation of topography, atmospheric dust, microphysical scheme, and vertical remapping, as well as the inclusion of a non-orographic gravity wave parameterization<sup>53</sup>. CESM1 WACCM has an internally generated quasi-biennial oscillation and a very good representation of stratospheric dynamics and transport. CESM1(WACCM) utilizes the Modal Aerosol Model (MAM3)<sup>55</sup>, which can simulate the formation of stratospheric sulfate aerosols after injection of  $\text{SO}_2$ , as well as microphysical growth and sedimentation<sup>53,56</sup>. CESM1(WACCM) includes fully interactive middle atmosphere chemistry, with 95 solution species, two invariant species, 91 photolysis reaction and 207 other reactions., CESM1(WACCM) uses the Parallel Ocean Program (POP2) for the ocean model<sup>57</sup> and the Los Alamos Sea Ice Model (CICE4)<sup>58</sup>. CESM1(WACCM) version used here utilizes the Community Land Model, version 4.5 (CLM4.5)<sup>59</sup>. CESM1(WACCM) was evaluated in Mills et al.<sup>53</sup> for studies of aerosol-climate interactions by

comparing the model's response against observations following historical volcanic eruptions. The study found that CESM1(WACCM) accurately calculates radiative and chemical responses to stratospheric sulfate, confirming the validity of its use for solar geoengineering studies.

GLENS employs the use of a large ensemble approach with a 20-member ensemble of simulations with stratospheric  $\text{SO}_2$  injections, and 20-member ensemble of RCP8.5 controls for years 2010 and 2030, with 3 of those members extended to at least 2097.  $\text{SO}_2$  injections in the geoengineering simulations were calculated by a feedback or control algorithm. MacMartin et al.<sup>60</sup> specified the annually varying amount of  $\text{SO}_2$  injection at four latitudes ( $15^\circ\text{S}$ ,  $15^\circ\text{N}$ ,  $30^\circ\text{S}$ ,  $30^\circ\text{N}$ ) to best meet the surface temperature targets. Injections are spread evenly over the entire year and recalculated by the feedback control algorithm to be able to smoothly push climate without causing abrupt changes. The goal of GLENS is to maintain global, interhemispheric, and equator-to-pole surface temperatures at levels consistent with the year 2020 under the RCP8.5 (Representative Concentration Pathway) scenario<sup>28</sup>, (Supplementary Fig. 1). Note that no volcanic eruptions are assumed for the future under this scenario. In Tilmes et al.<sup>28</sup>, geoengineering runs are referred to as the “Feedback” simulations, (<https://www.cesm.ucar.edu/projects/community-projects/GLENS/>) whereas here, we simply refer to them as “Geoengineering”. Twenty geoengineering ensemble members were initialized from the year 2020 of the RCP8.5 simulations and integrated until the end of the century at 2100 (Supplementary Table S1). The availability of 20 ensemble members of RCP8.5 for the 2010–2030 period allows for comprehensive comparison of geoengineering to this control period. All analyses presented here include all available ensemble members and years. Annual surface temperature and precipitation, and cool season precipitation climatology are computed using monthly mean model output. The historical simulation validation is discussed in Tilmes et al.<sup>28</sup> and Mills et al.<sup>53</sup>. Specifically, globally averaged annual surface temperatures compared to HadCRUT4 and GISTEMP reconstructions (Supplementary Fig. S6) are adapted from Mills et al.<sup>53</sup>, Fig. 1.

### AR identification

Currently, there are many ARDTs (Atmospheric River Detection Tools) available to the community, each designed for a specific purpose and science question. Consequently, common AR metrics, such as AR counts and intensities, have a large uncertainty associated with them, as shown by the Atmospheric River Tracking Method Intercomparison Project<sup>14,39,61,62</sup>. The method applied here is the Shields/Kiehl method<sup>15,46,47</sup> and was originally designed to isolate stronger moisture streams relative to their background environment, thus, effectively removing thermodynamic influences on AR counts solely reflective of the Clausius-Clapeyron

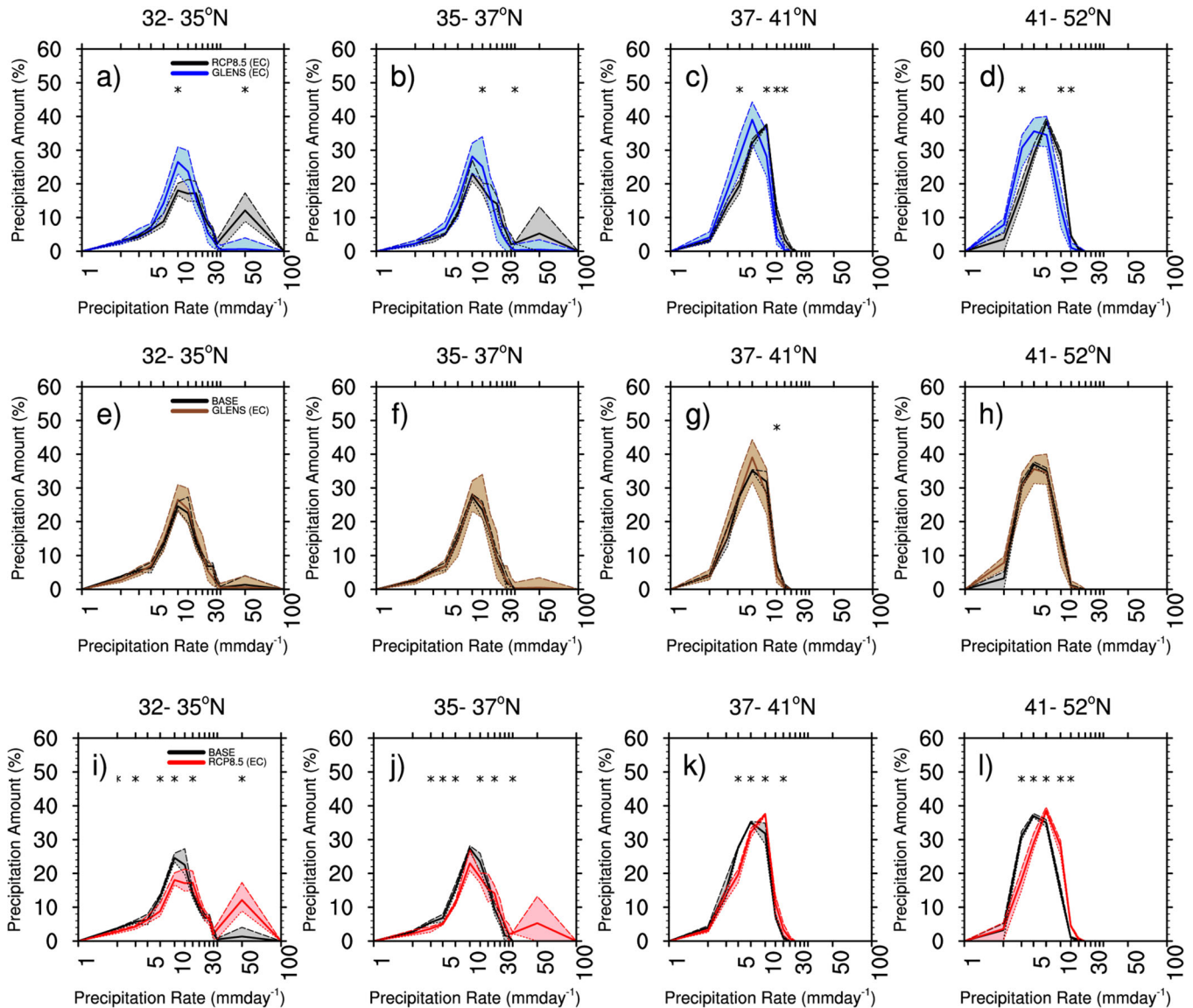


**Fig. 5 Pineapple Express AR precipitation intensity rates.** Pineapple Express AR precipitation intensity rates (x-axis,  $\text{mmday}^{-1}$ ) and rain amount (%) for GLENS end of century (EC) (blue/light blue) compared to RCP8.5 (EC) (black/gray) (a–d), GLENS (EC) (brown/tan) compared to BASE (black/gray) (e–h), RCP8.5 (EC) (red/pink) compared to BASE (black/gray) (i–l). Black and gray in each grouping are used to denote the reference period consistent with Figs. 2–4 and are given different color-themes to highlight analysis scenarios. For example, the blue lines in a–d are the same as black lines in i–l. Lighter colors and shading represent ensemble spread, long dashes represent maximum value, small dashes represent minimum value, and starred markers above each curve show significance where there is no overlap in ensemble spread between analysis periods compared. Precipitation is averaged across 110–130°W for latitudes 37–52°N and 116–130°W for latitudes 32–37°N.

relationship. Instead, this method focuses on dynamic changes produced by climate change. Among ARTMP algorithms, the Shields/Kiehl (hereafter referred to as SK2016) can be classified as a restrictive and relative (time-varying) ARDT. SK2016 defines moisture (integrated water vapor, IWV) thresholds as anomalies relative to its spatial environment using the empirical relationship defined by Zhu and Newell<sup>40</sup>, and used by Newman et al.<sup>63</sup> and Gorodetskaya et al.<sup>64</sup>, i.e., at each time interval, both zonal mean and maximum values for each latitude are computed to determine if an AR condition exists for that grid point. Wind thresholds are computed separately using the low-level wind vector at the 85th percentile wind magnitude for the region of application, following methodology from Lavers et al.<sup>65</sup>. Here, we focus on western North America between 32°N and 52°N, and in addition to applying moisture and wind thresholds, we restrict ARs to those ultimately making landfall and originating from the southwest quadrant (i.e., the “Pineapple Express” AR flavor). Geometry requirements are also applied such that the AR object must be longer than wide (2:1 ratio) and a minimum of 200 km in length. It is also important to note that SK2016

does not define a spatial footprint, rather, the ARDT saves all IWV and wind domain information at the timestep of landfall so that the source data, rather than the ARDT, defines the AR. This effectively sidesteps the thorny issue among ARDTs as to the characteristics of the spatial footprint, however, unfortunately, it is not easily compared to other ARDTs for metrics such as area and life cycle stages<sup>66</sup>. Comparisons on how it compares to ARTMP ARDTs for other common metrics can be found in Shields et al.<sup>61</sup> (precipitation, Fig. 7; intensity Fig. 6), Rutz et al.<sup>39</sup> (precipitation, Fig. 12; intensity, Fig. 9; frequency, Fig. 6), and Shields et al.<sup>67</sup> (meridional heat transport, Fig. 1). ARs are detected at 6-hourly intervals and precipitation attributable to ARs is computed using 6-hourly data.

### Limitations

Increasing ensemble members for the RCP8.5 end of century could potentially improve confidence as well as higher horizontal resolution datasets. Because resolution dependencies affect AR frequencies and

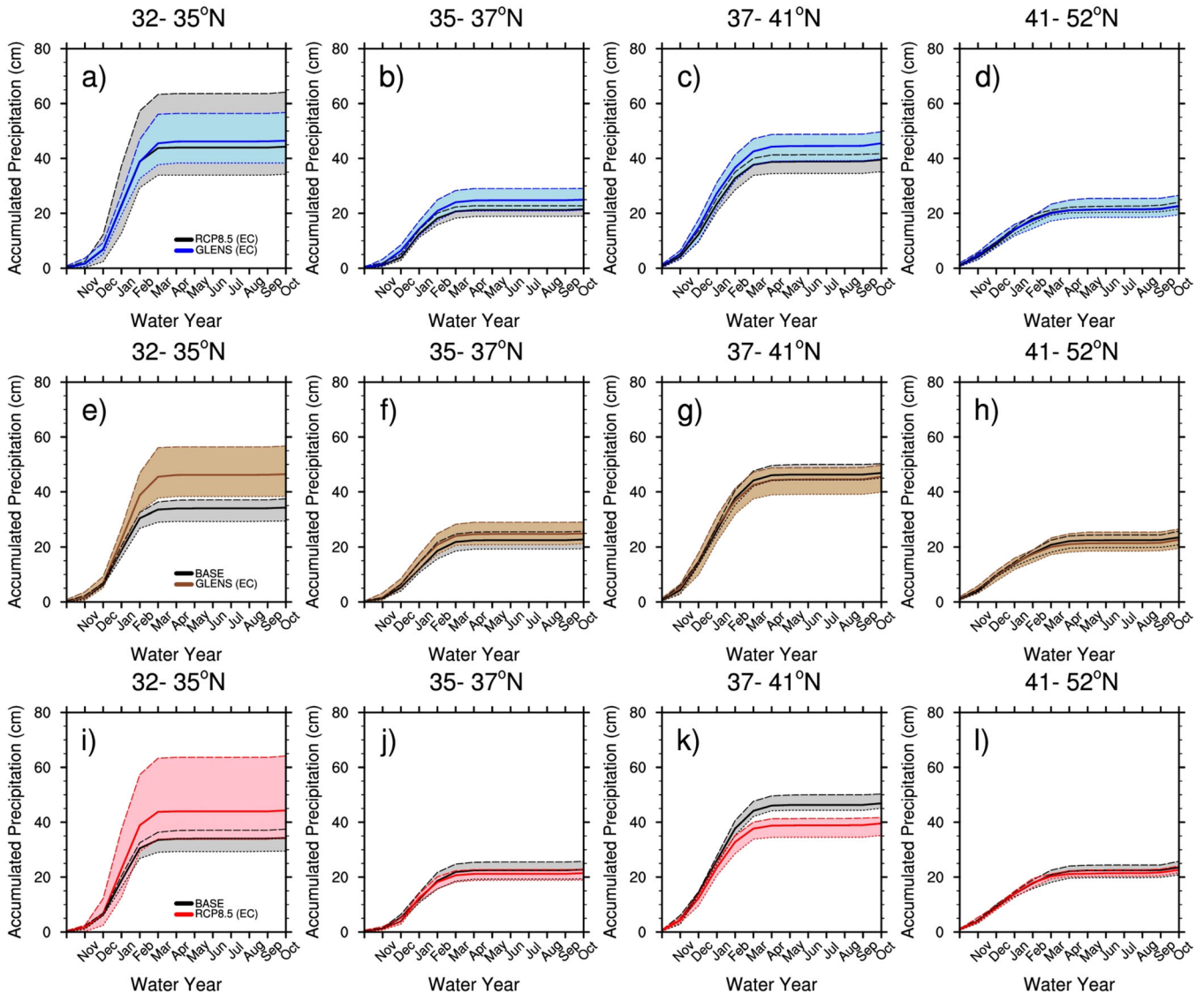


**Fig. 6** Water year estimates for Pineapple Express ARs. Mean water year and ensemble range (x-axis,  $\text{mmday}^{-1}$ ) for accumulated Pineapple Express AR-precipitation amount (cm) for GLENS end of century (EC) (blue/light blue) compared to RCP8.5 (EC) (black/gray) (a–d), GLENS (EC) (brown/tan) compared to BASE (black/gray) (e–h), RCP8.5 (EC) (red/pink) compared to BASE (black/gray) (i–l). Color organization for scenario comparisons and precipitation area means are the same as for Fig. 5.

characteristics<sup>13,62,68,69</sup>, using a  $\sim 1^\circ$  latitude and longitude spacing is another potential limitation and cause for caution. For SK2016 ARDT, high resolution translates into fewer ARs, although this is not the case for other ARDTs, such as algorithms with different geometric considerations (Reid et al., 2020). Typically, high resolution is better suited for AR studies, in particular for precipitation attribution, because high resolution more accurately represents the hydrological cycle and the topographical features important for AR forcing. Using a regionally refined CESM framework, Rhoades et al.<sup>13</sup> shows the importance of high horizontal resolution in the North Pacific when characterizing landfalling AR and orographic precipitation. Additionally, Shields et al.<sup>70</sup>, demonstrates that moving from a  $1^\circ$  to  $0.5^\circ$  horizontal grid spacing effectively changes the sign global warming signal for the large-scale precipitation in the American Southwest. Horizontal resolution also affects the placement of the eddy and subtropical jets which can profoundly affect AR landfalling locations given the reliance on the low-level winds<sup>68,71</sup>. This can be illustrated by Shields and Kiehl<sup>46</sup> where the  $0.5^\circ$  resolution produces a different pattern of AR frequency changes over Southern California under RCP8.5 and is simply due to the different placement of the low-level jet between resolutions. Finally, the use of one ARDT is also a limitation given that ARTMIP has shown that uncertainty among algorithms is high, especially for climate change<sup>2,14,39</sup>. Comparison of SK2016 to other ARTMIP metrics is discussed in the AR Identification section.

#### DATA AVAILABILITY

CESM model data from the GLENS project is available at <https://www.cesm.ucar.edu/projects/community-projects/GLENS/>. AR tracking data files and analysis data is available via the NCAR GDEX (Geoscience Data Exchange) services, <https://doi.org/10.5065/mjs1-k131>.

#### CODE AVAILABILITY

CESM model data is publicly available at <https://www.cesm.ucar.edu/>. Code used for AR tracking and analysis is available upon request at shields@ucar.edu.

Received: 10 November 2021; Accepted: 5 April 2022;

Published online: 18 May 2022

#### REFERENCES

1. Ralph, F. M., Dettinger, M. D., Cairns, M. M., Galarneau, T. J. & Eyrander, J. Defining “atmospheric river”: how the glossary of meteorology helped resolve a debate, *bull. Bull. Am. Meteorol. Soc.* **99**, 837–839 (2018).



2. Payne, A. E. et al. Responses and impacts of atmospheric rivers to climate change. *Nat. Rev. Earth Environ.* **1**, 143–157 (2020).
3. Gimeno, L. et al. The residence time of water vapour in the atmosphere. *Nat. Rev. Earth Environ.* **2**, 558–569 (2021).
4. Gimeno, L., Nieto, R., Vázquez, M. & Lavers, D. A. Atmospheric rivers: a mini-review. *Front. Earth Sci.* **2**, 2 (2014).
5. Ralph, F. M., Neiman, P. J. & Wick, G. A. Satellite and CALJET aircraft observations of atmospheric rivers over the eastern North Pacific Ocean during the winter of 1997/98. *Mon. Wea. Rev.* **132**, 1721–1745 (2004).
6. Neiman, P. J., Ralph, F. M., Wick, G. A., Lundquist, J. & Dettinger, M. D. Meteorological characteristics and overland precipitation impacts of atmospheric rivers affecting the West Coast of North America based on eight years of SSM/I satellite observations. *J. Hydrometeorol.* **9**, 22–47 (2008).
7. Lavers, D. A. & Villarini, G. The contribution of atmospheric rivers to precipitation in Europe and the United States. *J. Hydrol.* **522**, 382–390 (2015).
8. Dettinger, Ralph, F. M., Das, T., Neiman, P. J. & Cayan, D. Atmospheric rivers, floods, and the water resources of California. *Water* **3**, 455–478 (2011).
9. Guan, B., Molotch, N. P., Waliser, D. E., Fetzer, E. J., & Neiman, P. J. Extreme snowfall events linked to atmospheric rivers and surface air temperature via satellite measurements. *Geophys. Res. Lett.* **37**, L20401 (2010).
10. Dettinger, M. D. Atmospheric rivers as drought busters on the US West Coast. *J. Hydrometeorol.* **14**, 1721–1732 (2013).
11. Corringham, T. W., Ralph, F. M., Gershunov, A., Cayan, D. R. & Talbot, C. A. Atmospheric rivers drive flood damages in the western United States. *Sci. Adv.* **5**, eaax4631 (2019).
12. Gershunov, A. et al. Precipitation regime change in Western North America: the role of Atmospheric Rivers. *Sci. Rep.* **9**, 1–11 (2019).
13. Rhoades, A. M., Risser, M. D., Stone, D. A., Wehner, M. F. & Jones, A. D. Implications of warming on western United States landfalling atmospheric rivers and their flood damages. *Weather Clim. Extremes* **32**, 100326 (2021).
14. O'Brien, et al. Increases in future AR count and size: overview of the ARTMIP tier 2 CMIP5/6 experiment. *J. Geophys. Res. Atmos.*, **127**, e2021JD036013. <https://doi.org/10.1029/2021JD036013> (2022).
15. Shields, C. A. & Kiehl, J. T. Simulating the pineapple express in the half degree community climate system model, CCSM4. *Geophys. Res. Lett.* **43**, 7767–7773 (2016).
16. Espinoza, V., Waliser, D. E., Guan, B., Lavers, D. A. & Ralph, F. M. Global analysis of climate change projection effects on atmospheric rivers. *Geophys. Res. Lett.* **45**, 4299–4308 (2018).
17. Lavers, D. A., Ralph, F. M., Waliser, D. E., Gershunov, A. & Dettinger, M. D. Climate change intensification of horizontal water vapor transport in CMIP5. *Geophys. Res. Lett.* **42**, 5617–5625 (2015).
18. Trenberth, K. E. & Dai, A. Effects of Mount Pinatubo volcanic eruption on the hydrological cycle as an analog of geoengineering. *Geophys. Res. Lett.* **34**, L15702 (2007).
19. Kiehl, J. T. Geoengineering climate change: treating the symptom over the cause? *Clim. Change* **77**, 227 (2006).
20. Huttunen, S. & Hildén, M. Framing the controversial: geoengineering in academic literature. *Sci. Commun.* **36**, 3–29 (2014).
21. Pamplany, A., Gordijn, B. & Brereton, P. The ethics of geoengineering: a literature review. *Sci. Eng. Ethics* **26**, 3069–3119 (2020).
22. National Academies of Sciences, Engineering, and Medicine. *Reflecting sunlight: recommendations for solar geoengineering research and research governance* (The National Academies Press, 2021) <https://doi.org/10.17226/25762>.
23. Kravitz, B. et al. The Geoengineering Model Intercomparison Project (GeoMIP). *Atmos. Sci. Lett.* **12**, 162–167 (2011).
24. Kravitz, B. et al. An energetic perspective on hydrological cycle changes in the Geoengineering Model Intercomparison Project (GeoMIP). *J. Geophys. Res.* **118**, 13087–13102 (2013).
25. Tilmes, S. et al. A new Geoengineering Model Intercomparison Project (GeoMIP) experiment designed for climate and chemistry models. *Geosci. Model Dev.* **8**, 43–49 (2015).
26. Visioni, D. et al. Reduced poleward transport due to stratospheric heating under stratospheric aerosols geoengineering. *Geophys. Res. Lett.* **47**, e2020GL089470 (2020).
27. Kravitz, B. et al. First simulations of designing stratospheric sulfate aerosol geoengineering to meet multiple simultaneous climate objectives. *J. Geophys. Res. Atmos.* **122**, 12,616–12,634 (2017).
28. Tilmes, S. et al. CESM1(WACCM) Stratospheric Aerosol Geoengineering Large Ensemble Project. *Bull. Am. Meteorological Soc.* **99**, 2361–2371 (2018).
29. Deser, C., Phillips, A. S., Alexander, M. A. & Smoliak, B. V. Projecting North American climate over the next 50 years: uncertainty due to internal variability. *J. Clim.* **27**, 2271–2296 (2014).
30. Kay, J. E. et al. The Community Earth System Model (CESM) large ensemble project: a community resource for studying climate change in the presence of internal climate variability. *Bull. Am. Meteorological Soc.* **96**, 1333–1349 (2015).
31. Richter, J. H. et al. Stratospheric dynamical response and ozone feedbacks in the presence of SO<sub>2</sub> injections. *J. Geophys. Res. Atmospheres* **122**, 12,557–12,573 (2017).
32. Tilmes, S. et al. The hydrological impact of geoengineering in the Geoengineering Model Intercomparison Project (GeoMIP). *J. Geophys. Res. Atmos.* **118**, 11036–11058 (2013).
33. Fasullo, J. T. et al. Persistent polar ocean warming in a strategically geoengineered climate. *Nat. Geosci.* **11**, 910–914 (2018).
34. Jiang, J. et al. Stratospheric sulfate aerosol geoengineering could alter the high-latitude seasonal cycle. *Geophys. Res. Lett.* **46**, 14153–14163 (2019).
35. Cheng, W. et al. Soil moisture and other hydrological changes in a stratospheric aerosol geoengineering large ensemble. *J. Geophys. Res. Atmos.* **124**, 12773–12793 (2019).
36. Simpson, I. R. et al. The regional hydroclimate response to stratospheric sulfate geoengineering and the role of stratospheric heating. *J. Geophys. Res. Atmospheres* **124**, 12587–12616 (2019).
37. Karami, K., Tilmes, S., Muri, H. & Mousavi, S. V. Storm track changes in the Middle East and North Africa under stratospheric aerosol geoengineering. *Geophys. Res. Lett.* **47**, e2020GL086954 (2020).
38. Da-Allada, C. Y. et al. Changes in west African summer monsoon precipitation under stratospheric aerosol geoengineering. *Earth Future* **8**, e2020EF001595 (2020).
39. Rutz, J. J. et al. The Atmospheric River Tracking Method Intercomparison Project (ARTMIP): quantifying uncertainties in atmospheric river climatology. *J. Geophys. Res. Atmos.* **124**, 13777–13802 (2019).
40. Zhu, Y. & Newell, R. E. A proposed algorithm for moisture fluxes from atmospheric rivers. *Mon. Weather Rev.* **126**, 725–735 (1998).
41. Harvey, B. J., Cook, P., Shaffrey, L. C. & Schiemann, R. (2020), The response of the northern hemisphere storm tracks and jet streams to climate change in the CMIP3, CMIP5, and CMIP6 climate models. *J. Geophys. Res. Atmos.* **125**, e2020JD032701 (2020).
42. Shaw, T. A. Mechanisms of future predicted changes in the zonal mean mid-latitude circulation. *Curr. Clim. Change Rep.* **5**, 345–357 (2019).
43. Yin, J. H. A consistent poleward shift of the storm tracks in simulations of 21st century climate. *Geophys. Res. Lett.* **32**, L18701 (2005).
44. Payne, A. E. & Magnusdottir, G. An evaluation of atmospheric rivers over the North Pacific in CMIP5 and their response to warming under RCP 8.5. *J. Geophys. Res. Atmos.* **120**, 11,173–11,190 (2015).
45. Barnes, E. A. & Polvani, L. Response of the midlatitude jets, and of their variability, to increased greenhouse gases in the CMIP5 models. *J. Clim.* **26**, 7117–7135 (2013).
46. Shields, C. A. & Kiehl, J. T. Atmospheric river landfall-latitude changes in future climate simulations. *Geophys. Res. Lett.* **43**, 8775–8782 (2016).
47. Shields, C. A., Kiehl, J. T., Rush, W., Rothstein, M. & Snyder, M. A. (2021), Atmospheric rivers in high-resolution simulations of the Paleocene Eocene Thermal Maximum (PETM). *Palaeogeogr. Palaeoclimatol. Palaeoecol.* **567**, 110293 (2021).
48. Tabor, C. et al. A mechanistic understanding of oxygen isotopic changes in the Western United States at the last glacial maximum. *Quat. Sci. Rev.* **274**, 107255 (2021).
49. Wallace, J. M., & Hobbs, P. V. *Atmospheric science: an introductory survey* (Elsevier Academic Press, 2006).
50. Gimeno, L., Algarra, I., Eiras-Barca, J., Ramos, A. M. & Nieto, R. Atmospheric River, a term encompassing different meteorological patterns. *Wiley Interdiscip. Rev. Water* **8**, e1558 (2021).
51. Shields, C. A. et al. Defining uncertainties through comparison of atmospheric river tracking methods. *Bull. Am. Meteorol. Soc.* **100**, ES93–ES96 (2019).
52. Dacre, H. F., Clark, P. A., Martinez-Alvarado, O., Stringer, M. A. & Lavers, D. A. Lavers How do atmospheric rivers form? *Bull. Am. Meteor. Soc.* **96**, 1243–1255 (2015).
53. Mills, M. J. et al. Radiative and chemical response to interactive stratospheric sulfate aerosols in fully coupled CESM1(WACCM). *J. Geophys. Res. Atmos.* **122**, 13 061–13 078 (2017).
54. Neale, R. B. et al. *Description of the NCAR Community Atmosphere Model (CAM 5.0)*. Technical Report NCAR/TN-4861STR, (NCAR, 2010).
55. Liu, X. et al. Toward a minimal representation of aerosols in climate models: description and evaluation in the Community Atmosphere Model CAM5. *Geosci. Model Dev.* **5**, 709–739 (2012).
56. Mills, M. J. et al. Global volcanic aerosol properties derived from emissions, 1990–2014, using CESM1(WACCM). *J. Geophys. Res. Atmos.* **121**, 2332–2348 (2016).
57. Danabasoglu, G. et al. The CCSM4 ocean component. *J. Clim.* **25**, 1361–1389 (2012).
58. Holland, M. The great sea-ice dwindle. *Nat. Geosci.* **6**, 10–11 (2013).
59. Oleson, K. et al. *Technical description of version 4.5 of the Community Land Model (CLM)*. Technical Report NCAR/TN-503+STR, 422 (National Center for Atmospheric Research, 2017).

60. MacMartin, D. G. et al. The climate response to stratospheric aerosol geoengineering can be tailored using multiple injection locations. *J. Geophys. Res. Atmos.* **122**, 12–574 (2017).
61. Shields, C. A. et al. Atmospheric River Tracking Method Intercomparison Project (ARTMIP): project goals and experimental design. *Geosci. Model Dev.* **11**, 2455–2474 (2018).
62. Collow, A. B. M. et al. An overview of ARTMIP's tier 2 reanalysis intercomparison: uncertainty in the detection of atmospheric rivers and their associated precipitation. *J. Geophys. Res. Atmos.* **127**, e2021JD036155 (2022).
63. Newman, M., Kiladis, G. N., Weickmann, K. M., Ralph, F. M. & Sardeshmukh, P. D. Relative contributions of synoptic and low-frequency eddies to time-mean atmospheric moisture transport, including the role of atmospheric rivers. *J. Clim.* **25**, 7341–7361 (2012).
64. Gorodetskaya, I. V. et al. The role of atmospheric rivers in anomalous snow accumulation in East Antarctica. *Geophys. Res. Lett.* **41**, 6199–6206 (2014).
65. Lavers, D. A., Villarini, G., Allan, R. P., Wood, E. F. & Wade, A. J. The detection of atmospheric rivers in atmospheric reanalyses and their links to British winter floods and the large-scale climatic circulation. *J. Geophys. Res. Atmos.* **117**, D20106 (2012).
66. Zhou, Y. et al. Uncertainties in atmospheric river lifecycles by detection algorithms: climatology and variability. *J. Geophys. Res. Atmos.* **126**, e2020JD033711 (2021).
67. Shields, C. A. et al. Meridional heat transport during atmospheric rivers in high-resolution CESM climate projections. *Geophys. Res. Lett.* **46**, 14702–14712 (2019).
68. Hagos, S. M., Ruby Leung, L., Yang, Q., Zhao, C. & Lu, J. Resolution and dynamical core dependence of atmospheric river frequency in global model simulations. *J. Clim.* **28**, 2764–2776 (2015).
69. Reid, K. J., King, A. D., Lane, T. P. & Short, E. The sensitivity of atmospheric river identification to integrated water vapor transport threshold, resolution, and regridding method. *J. Geophys. Res. Atmos.* **125**, e2020JD032897 (2020).
70. Shields, C. A., Kiehl, J. T. & Meehl, G. A. Future changes in regional precipitation simulated by a half-degree coupled climate model: Sensitivity to horizontal resolution. *J. Advn Model. Earth Syst.* **8**, 863–884 (2016).
71. Lu, J. et al. Toward the dynamical convergence on the jet stream in aquaplanet AGCMs. *J. Clim.* **28**, 6763–6782 (2015).

## ACKNOWLEDGEMENTS

This work was supported by the National Center for Atmospheric Research (NCAR), which is a major facility sponsored by the National Science Foundation (NSF) under Cooperative Agreement 1852977 and by SilverLining through its Safe Climate Research Initiative. The Community Earth System Model (CESM) project is supported primarily by the National Science Foundation. Computing and data storage resources, including the Cheyenne supercomputer (doi:10.5065/D6RX99HX), were provided by the Computational and Information Systems Laboratory (CISL) at NCAR. We thank Sasha Glanville, Michael Mills, and Adam Phillips for their contributions recreating

supplemental figures, and processing model data. We also thank reviewers Alan Rhoades and an anonymous reviewer for helpful comments and improving this paper.

## AUTHOR CONTRIBUTIONS

C.A.S. contributions include writing (primary), analysis, and figures; J.H.R. contributions include writing (GLENS), figures, and writing/geoengineering guidance; A.P. contributions include analysis (precipitation), writing/guidance, and S.T. contributions include the GLENS simulations and writing/geoengineering guidance.

## COMPETING INTERESTS

The authors declare no competing interests.

## ADDITIONAL INFORMATION

**Supplementary information** The online version contains supplementary material available at <https://doi.org/10.1038/s41612-022-00260-8>.

**Correspondence** and requests for materials should be addressed to Christine A. Shields.

**Reprints and permission information** is available at <http://www.nature.com/reprints>

**Publisher's note** Springer Nature remains neutral with regard to jurisdictional claims in published maps and institutional affiliations.



**Open Access** This article is licensed under a Creative Commons Attribution 4.0 International License, which permits use, sharing, adaptation, distribution and reproduction in any medium or format, as long as you give appropriate credit to the original author(s) and the source, provide a link to the Creative Commons license, and indicate if changes were made. The images or other third party material in this article are included in the article's Creative Commons license, unless indicated otherwise in a credit line to the material. If material is not included in the article's Creative Commons license and your intended use is not permitted by statutory regulation or exceeds the permitted use, you will need to obtain permission directly from the copyright holder. To view a copy of this license, visit <http://creativecommons.org/licenses/by/4.0/>.

© The Author(s) 2022